Editors' Suggestion

# Roton Excitations in an Oblate Dipolar Quantum Gas

J.-N. Schmidt,[1] J. Hertkorn,[1] M. Guo,[1] F. Böttcher,[1] M. Schmidt,[1] K. S. H. Ng,[1] S. D. Graham,[1] T. Langen,[1] M. Zwierlein,[2] and T. Pfau[1,*]

[1]*5. Physikalisches Institut and Center for Integrated Quantum Science and Technology, Universität Stuttgart, Pfaffenwaldring 57, 70569 Stuttgart, Germany*

[2]*MIT-Harvard Center for Ultracold Atoms, Research Laboratory of Electronics, and Department of Physics, Massachusetts Institute of Technology, Cambridge, Massachusetts 02139, USA*

(Received 2 February 2021; accepted 2 April 2021; published 12 May 2021)

We observe signatures of radial and angular roton excitations around a droplet crystallization transition in dipolar Bose-Einstein condensates. *In situ* measurements are used to characterize the density fluctuations near this transition. The static structure factor is extracted and used to identify the radial and angular roton excitations by their characteristic symmetries. These fluctuations peak as a function of the interaction strength indicating the crystallization transition of the system. We compare our observations to a theoretically calculated excitation spectrum allowing us to connect the crystallization mechanism with the softening of the angular roton modes.

DOI: 10.1103/PhysRevLett.126.193002

The roton dispersion relation is essential to understand the thermodynamics and density fluctuations in superfluid helium [1–4]. Initially interpreted by Feynman as the "ghost of a vanishing vortex ring" [5], nowadays the roton is seen as a precursor to the crystallization of a system [6]. Quantum gases with dipolar interactions feature a similar dispersion relation due to the anisotropic and long-range nature of their interaction [7,8]. In contrast to helium, the high tunability of atomic quantum gases allows for systematic studies of roton excitations. Tuning interatomic interactions can soften the rotons, which trigger an instability and the formation of a crystal of quantum droplets [9–11]. For elongated systems confined in cigar-shaped traps, this softening leads to the emergence of one-dimensional (1D) supersolid states that simultaneously exhibit superfluid flow and crystalline order [12–17].

In cylindrically symmetric oblate traps, two types of roton excitations have been predicted to play a crucial role in the instability [18–20]. These two modes are the radial and angular roton modes corresponding to the two spatial degrees of freedom in the system. The spectrum of these two-dimensional (2D) modes is more complex than the spectrum of a previously studied elongated 1D supersolid [21], making it a challenge to distinguish their individual contributions to the crystallization. While the roton modes were directly observed in 1D dipolar systems [22–24], the various angular roton modes in 2D and their connection to the crystallization have remained elusive.

In this Letter, we observe signatures of radial and angular roton excitations of an oblate dipolar Bose-Einstein condensate (BEC) around the phase transition to a 2D droplet crystal. These excitations leave their imprint in the density fluctuations of the gas, which we measure *in situ*, giving us direct access to the static structure factor $S(\boldsymbol{k})$ [21,25]. The quantity $S(\boldsymbol{k})$ features a peak at finite momentum and a distinct sixfold angular symmetry upon approaching the crystallization transition. We use mean-field simulations of the excitation spectrum to interpret the experimental results. The observed emergence of angular structure is thereby directly linked to the softening of angular roton modes.

The excitation spectrum of dipolar BECs in cylindrically symmetric traps can be theoretically studied in the Bogoliubov–de Gennes (BdG) framework. We solve the BdG equations including the first beyond mean-field correction [21,26] term known as the Lee-Huang-Yang (LHY) correction using our experimental parameters [27]. We calculate the excitation spectrum of the low-lying modes in the BEC up to the point of the instability of $15 \times 10^3$ $^{162}$Dy atoms in a trap as a function of the scattering length. The trapping frequencies are $\omega/2\pi = [35, 35.1, 110]$ Hz and the magnetic field points along $\hat{z}$. The trap geometry is deliberately made asymmetric to numerically lift the degeneracy in the $x - y$ direction [44]. The radial and angular roton modes found in these spectra can soften by varying the scattering length to energies much smaller than the trap frequencies [18–20,26].

The mode patterns of the density fluctuation $\delta n(\boldsymbol{r})$ corresponding to the radial and angular roton modes are shown in Fig. 1(a). We additionally present the spatial power spectra of the mode patterns given by the squared modulus of the Fourier transform $|\mathcal{F}[\delta n]|^2(\boldsymbol{k})$ illustrating the individual contributions to the static structure factor [24,45–49]. Radial roton modes are circularly symmetric and represent ringlike density modulations at nonzero radial wave vector. Angular rotons have an angular

 

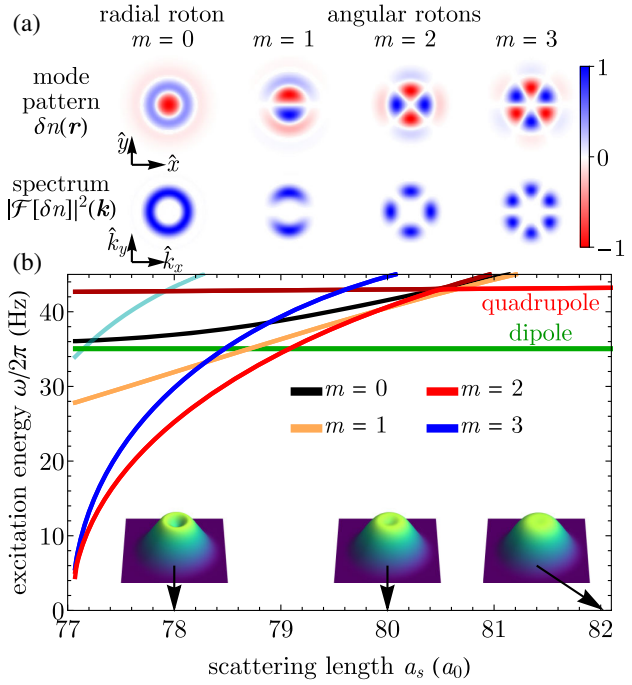


FIG. 1. (a) Normalized mode patterns of the density fluctuations close to the transition at $a_s \simeq 77.5a_0$ and their spatial power spectra in the $x$-$y$ plane. Shown are the lowest radial ($m = 0$) and angular rotons ($m = 1$, 2, 3) having $m$ angular nodal lines. (b) Corresponding Bogoliubov excitation energies as a function of the scattering length $a_s$, with the insets indicating the emergence of a blood cell shape in the ground-state density close to the instability at $a_s \simeq 77.1a_0$. For decreasing scattering lengths, first the $m = 2$ followed by the $m = 1$ and $m = 3$ angular roton modes drops below the radial dipole modes at the trap frequency and softens further toward the instability. For information on higher modes (e.g., cyan line) and details, see Refs. [27,50].

oscillatory structure in addition to the ringlike radial density modulation. We describe the angular oscillation with $\sin(m\phi)$, where $\phi$ is the azimuthal angle, and the integer $m > 0$ counts the number of nodal lines in the mode pattern. The spatial power spectrum of a mode with $m$ nodal lines has a $2m$-fold symmetry resulting in a four- and sixfold symmetric power spectrum for the $m = 2$ and $m = 3$ angular roton modes, respectively. In contrast, the quadrupole mode and higher-lying phonon modes might feature similar azimuthal symmetries but at smaller radial wave vector.

In Fig. 1(b), we show the low-lying excitation energies and ground-state shapes from the BEC side as a function of the scattering length toward the phase transition point [51]. In the BEC regime at high scattering lengths $a_s \simeq 81a_0$, farthest away from the transition point, the dipole mode has the lowest excitation energy and lies at exactly the trap frequency [52]. For decreasing scattering lengths, several higher-lying modes rapidly decrease in energy. These are the radial and twice degenerate angular roton modes. At around $a_s \simeq 79.1a_0$, the $m = 2$ mode drops below the trap frequency followed by the $m = 1$ and $m = 3$ modes. Near the phase transition point at $a_s \simeq 77.1a_0$, the $m = 2$ mode is only separated by a few Hz from the $m = 3$ mode. The ordering of the angular roton modes close to the phase transition point depends on a nontrivial interplay between the trap aspect ratio and the interaction strength [53].

Near $a_s \simeq 80.5a_0$, the parabola-shaped BEC ground state transforms into a biconcave blood-cell-like shape, which forms as it is energetically favorable in cylindrical geometries to push part of the density to the outer rim. This further enhances the softening of angular rotons as they become excitations of the ring-shaped region of maximal density [18]. Previous studies of blood-cell-shaped ground states [18–20,26,47,53–57] did not include the LHY correction that has since been shown to stabilize the system against collapse [58]. We also find it to enlarge the parameter regime for blood-cell-shaped ground states by a range in scattering length of approximately $1a_0$.

We experimentally study the emergence of the angular rotons with a dipolar BEC with typically $15 \times 10^3$ $^{162}$Dy atoms at a temperature $T \simeq 20$ nK. We adjust the crossed optical dipole trap after evaporation to an almost cylindrical trap with trapping frequencies $\omega/2\pi = [35(1), 37(1), 110(1)]$ Hz and the magnetic field along $\hat{z}$ [27]. In the magnetic field range around 30 G that we employ, lower three-body losses lead to droplet crystal lifetimes on the order of 200 ms after crossing the phase transition, which is an increase by a factor of 10 compared to previous experiments at similar densities [13,27]. We image the cloud *in situ* with a resolution of 1 $\mu$m and repeat the experiment around 200 times for a statistical analysis of the atomic densities. We further quote all scattering lengths relative to a reference scattering length $a_{\mathrm{ref}} = 91(10)a_0$ corresponding to the transition point because of an overall systematic shift in our scattering length calibration [27].

We then extract the static structure factor, which connects the spectrum of elementary excitations to the major contributing modes in the density fluctuations [24,45–49]. The intermediate steps of this analysis are shown in Fig. 2 for four distinct scattering lengths: in the BEC regime, closer to the transition, in the transition region, and for a droplet crystal.

First, we investigate the *in situ* densities $n_j(\boldsymbol{r})$ [Fig. 2(a)]. To remove residual contributions of the dipole mode, the center of mass of the atomic density distribution is taken as the origin. In addition, we postselect in an interval of $\pm 15\%$ with respect to the mean atom number at each scattering length [27]. We observe that the crystal structure is randomly oriented in individual images and consequently gets washed out when averaging over many images [Fig. 2(b)]. This highlights the continuous rotational symmetry breaking upon crossing the crystalline phase. In order to account for the randomly oriented crystal in the further analysis, we determine the individual rotation

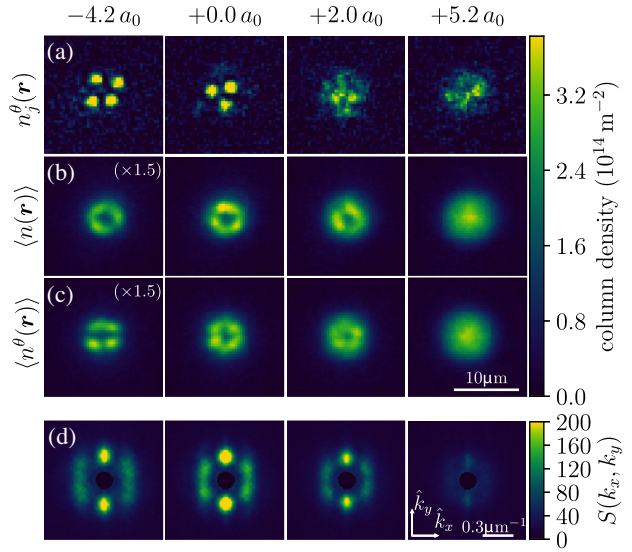


FIG. 2. (a) Single-shot images for four different relative scattering lengths, in the BEC regime ($+5.2a_0$), closer to the transition point ($+2.0a_0$), in the transition region ($+0.0a_0$), and for a droplet crystal ($-4.2a_0$). (b) Mean images of the unrotated images showing no clear crystalline structure. (c) Aligned images (see text) indicate the presence of droplets in the mean image. (d) 2D structure factor showing an increasing height of the peaks at finite momentum $|\boldsymbol{k}|$ indicating the approaching transition point. The central area below $k_{\mathrm{min}}/2\pi \simeq 0.11\ \mu\mathrm{m}^{-1}$ (see text) was masked out.

angles $\theta$ in Fourier space and align the single-shot images [27]. The rotated images $n_j^\theta(\boldsymbol{r})$ are used to create new mean images $\langle n^\theta(\boldsymbol{r})\rangle$, which reveal the emergence of the crystal structure [Fig. 2(c)]. As expected, the rotation does not affect the mean image in the BEC regime.

Second, we calculate the individual fluctuation patterns around this mean image $\delta n_j^\theta(\boldsymbol{r}) = n_j^\theta(\boldsymbol{r}) - \langle n^\theta(\boldsymbol{r})\rangle$ given by the deviations of the individual postselected and rotated images from the mean $\langle n^\theta(\boldsymbol{r})\rangle$. We determine the mean power spectrum $\langle|\delta n^\theta(\boldsymbol{k})|^2\rangle$ from a Fourier transform $\delta n_j^\theta(\boldsymbol{k}) = \int d^2r \delta n_j^\theta(\boldsymbol{r}) e^{i\boldsymbol{k}\cdot\boldsymbol{r}}$ of these fluctuation patterns. This mean power spectrum is closely connected to the static structure factor $S(\boldsymbol{k}) = \langle|\delta n^\theta(\boldsymbol{k})|^2\rangle/N$ for homogeneous systems [25,49,59] and also provides valuable insights into the nature of the excitations in nonhomogeneous systems [60–64].

The resulting 2D static structure factor $S(\boldsymbol{k})$ is shown in Fig. 2(d). We restrict the further analysis to momenta between $k_{\mathrm{min}}/2\pi \simeq 0.11\ \mu\mathrm{m}^{-1}$ and $k_{\mathrm{max}}/2\pi \simeq 1\ \mu\mathrm{m}^{-1}$ to account for the finite size of the cloud and the finite imaging resolution in the experiment [27]. The quantity $S(\boldsymbol{k})$ features several peaks that lie approximately on a ring with radius $|\boldsymbol{k}|$ around the origin. When approaching the transition point, the height of the individual peaks increases, and simultaneously the angular spreading of these peaks across the ring changes. In contrast, the angular distribution of $S(\boldsymbol{k})$ for unrotated images remains featureless, reflecting the symmetric trap. The enhancement of the peaks along the alignment axis ($\hat{\boldsymbol{y}}$ axis) is a result of the rotation algorithm, which always aligns the images according to their individual most dominant peak in Fourier space. Exploiting the cylindrical symmetry of the trap, we transform $S(\boldsymbol{k})$ to polar coordinates $S(k_x, k_y) \to S(k, \phi)$ and analyze its radial and angular behavior separately.

The radial behavior $S(k)$ is analyzed by integrating over the angular direction to identify modes at finite momentum $|\boldsymbol{k}|$ independent of their angular symmetry. The result is shown in Fig. 3(a) for scattering lengths around the transition. Starting in the BEC regime, we find $S(k)$ to be relatively flat with only a small peak at around $k/2\pi \simeq 0.22\ \mu\mathrm{m}^{-1}$. Closer to the transition, this peak rises and shifts toward larger momenta. We determine the center momentum $k_{\mathrm{rot}}$ and amplitude $S_{\mathrm{max}}$ of the peak using a Gaussian fit and show it in Figs. 3(b) and 3(c).

The peak of the structure factor $S_{\mathrm{max}}$ first increases with decreasing scattering lengths and then features a maximum before it decreases again. This is consistent with the

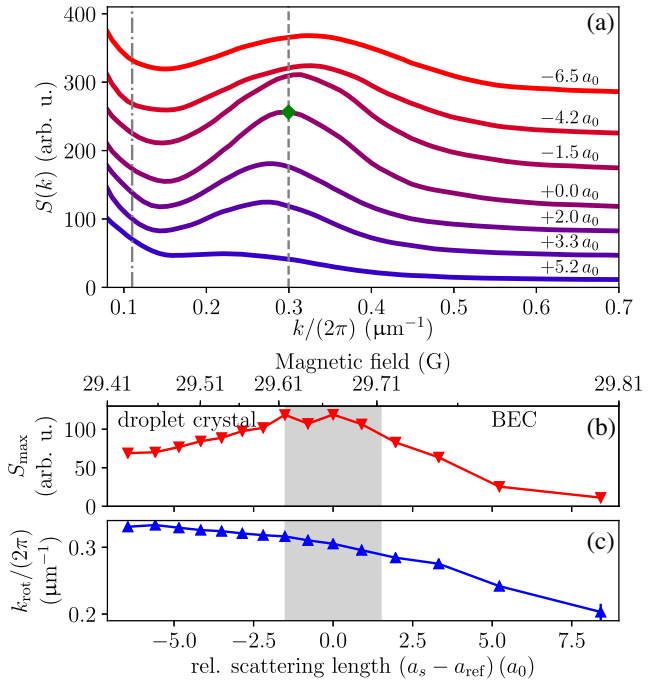


FIG. 3. (a) Radial distribution $S(k)$ of the two-dimensional structure factor after integration over the angular coordinate for different relative scattering lengths. A clear peak at finite wave vector rises toward the phase transition. For clarity, the lines for smaller scattering lengths were shifted vertically. (b) The amplitude of this peak is obtained from a Gaussian fit reaching its maximum at the phase transition. (c) Roton momentum shifts toward larger values in the droplet regime where it stays constant. The dash-dotted line on the left indicates the smallest momentum $k_{\mathrm{min}}/2\pi \simeq 0.11\ \mu\mathrm{m}^{-1}$. The green diamond indicates the maximum $S(k)$ and the dashed line the roton momentum at that maximum. The gray area in (b) and (c) indicates the transition region.

expectation of enhanced fluctuations at the phase transition due to the softening and thermal population of several roton modes close to the phase transition in a finite-sized system experiencing broadening due to hysteresis [13,24]. Compared to 1D, the increased number of low-lying excitations with different symmetries results in higher shot-to-shot fluctuations in 2D. From individual images, it is therefore more challenging to distinguish between an angular roton mode and a formed droplet crystal featuring the same symmetry. The formation of a droplet crystal is a direct consequence of the excitation of an angular roton mode with the same symmetry assuming a dynamical preparation scheme. We account for these uncertainties by marking a transition region $(+0.0 \pm 1.5)a_0$ rather than a single point [27]. In the droplet regime, the peak amplitude decreases and its position stays approximately constant at $k_{\mathrm{rot}}/2\pi \simeq 0.33\ \mu\mathrm{m}^{-1}$, which roughly indicates the inverse droplet distance. The peak also broadens further, indicating a competition between different droplet numbers and spacings.

The angular behavior $S(\phi)$ is obtained by integrating $S(k,\phi)$ over the annulus with $k \in [0.2, 0.45]\ \mu\mathrm{m}^{-1}$ [27]. $S(\phi)$ is shown in Fig. 4(a) and allows us to attribute the enhancement of the fluctuations to individual modes.

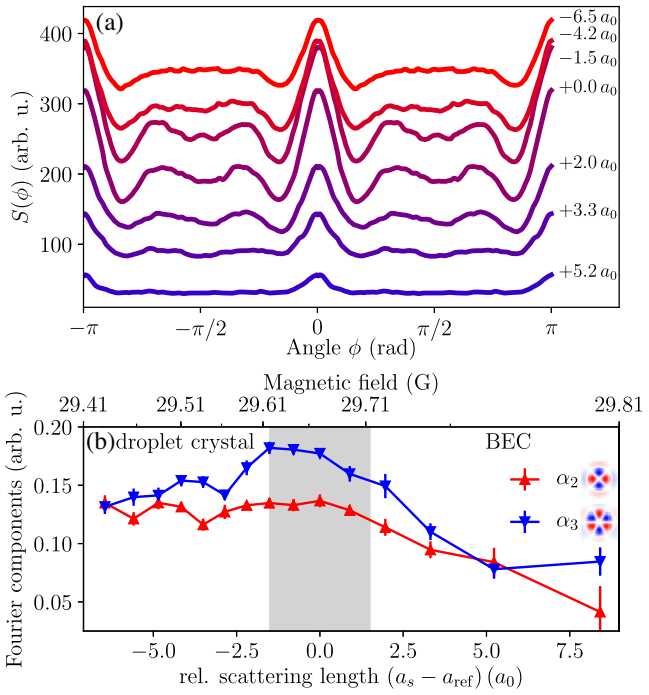


FIG. 4. (a) Angular distribution $S(\phi)$ of the two-dimensional static structure factor integrated over the interval $k/2\pi \in [0.2, 0.45]\ \mu\mathrm{m}^{-1}$ around the roton momentum $k_{\mathrm{rot}}$ for different relative scattering lengths. (b) Decomposition of $S(\phi)$ into Fourier components matching the symmetry of the lowest two angular roton modes $m = 2$ and $m = 3$ in the BEC. For clarity, the lines in (a) were shifted vertically for smaller scattering lengths. The gray area in (b) indicates the transition region. Error bars are obtained by bootstrapping [65].

Starting in the BEC regime, only two peaks at $\phi = 0$ and $\phi = \pi$ are visible which increase for lower scattering lengths. While they are still small compared to lower scattering lengths, these peaks can mainly be attributed to our rotation algorithm [27]. Closer to the transition, four additional peaks at $\phi = \pm\pi/3$ and $\phi = \pm 2\pi/3$ emerge to produce a rising sixfold symmetry indicative of the $m = 3$ angular roton mode. In the droplet regime, these intermediate peaks start to wash out, presumably due to the competition of the three- and four-droplet configurations.

We further quantify the changing mode population with lowest coefficients of a Fourier expansion of the normalized periodic function $S(\phi)/\max_\phi[S(\phi)]$. After normalization, the Fourier components shown in Fig. 4(b) describe the relative strength of the lowest two angular roton modes [27]. On the BEC side, the Fourier coefficients $\alpha_n$ give an indication of the underlying symmetry that then can be connected to the modes from the simulation of Fig. 1. We focus on the coefficients $\alpha_2$ and $\alpha_3$ which both have a low contribution in the BEC regime.

The increasing weights indicate a softening of several angular roton modes. The $\alpha_2$ and $\alpha_3$ modes increase toward the transition, in agreement with the simulation shown in Fig. 1(b). The $\alpha_2$ weight saturates near the transition and stays constant in the droplet regime. However, the $\alpha_3$ weight reaches a maximum after the transition and becomes smaller in the droplet regime. A stronger $\alpha_3$ weight than $\alpha_2$ is not supported by the presented theory if one assumes the population of those modes is in thermal equilibrium, as the $m = 2$ mode has a slightly lower energy than the $m = 3$ mode. This effect either hints toward nonequilibrium dynamics or toward the limits of the LHY approximation in the theoretical description [66–68].

In the crystalline domain, the two weights approach each other again, indicating that neither of the two angular roton modes are dominant. In this regime, $S(\boldsymbol{k})$ cannot be viewed as a measurement of excitations on top of the crystalline ground state because we find states with competing droplet numbers broadening the peak in the radial distribution of the 2D structure factor [see Fig. 3(a) and Ref. [27]]. Density patterns at single scattering lengths could have two to five droplets present in each shot (see Ref. [27]), indicating that the mean atomic density does not have the same symmetry as the ground state. Then, the weights $\alpha_i$ reflect the symmetry of the observed droplet crystal rather than an excitation on top of this crystalline ground state. The similarity of the $\alpha_2$ and $\alpha_3$ weights therefore indicates similar probabilities to find a droplet crystal with fourfold or sixfold symmetry.

In conclusion, we have reported on signatures of radial and angular roton modes by investigating the 2D static structure factor $S(\boldsymbol{k})$ of a dipolar BEC. The characteristic sixfold symmetry of $S(\boldsymbol{k})$ in the BEC regime can be identified with the population of the angular roton mode. These observations are supported by simulations of the

excitation spectrum. Our study has laid the foundation for a better understanding of the dominant excitations of dipolar BEC in oblate traps close to the transition to a droplet crystal. It connects the low-lying angular roton modes to the crystallization mechanism and the formation of droplets.

This work is supported by the German Research Foundation under Grants No. Bu2247/1, No. Pf381/20-1, No. FUGG INST41/1056-1, within the research group FOR2247 under Project No. Pf381/16-1, as well as by the Federal Ministry of Education and Research within the QUANT:ERA collaborative project MAQS under Grant No. 13N15231. M. G and M. Z acknowledge funding from the Alexander von Humboldt Foundation.

J.-N .S and J. H. contributed equally to this work.

*t.pfau@physik.uni-stuttgart.de

[1] L. Landau, Phys. Rev. **60**, 356 (1941).
[2] R. P. Feynman, Phys. Rev. **94**, 262 (1954).
[3] R. P. Feynman, Phys. Rev. **91**, 1291 (1953).
[4] R. P. Feynman and M. Cohen, Prog. Theor. Phys. **14**, 261 (1955).
[5] R. P. Feynman, *Application of Quantum Mechanics to Liquid Helium*, edited by C. Gorter (Elsevier, New York, 1955), Vol. 1, Chap. II, pp. 17–53.
[6] P. Nozières, J. Low Temp. Phys. **137**, 45 (2004).
[7] L. Santos, G. V. Shlyapnikov, and M. Lewenstein, Phys. Rev. Lett. **90**, 250403 (2003).
[8] M. Wenzel, F. Böttcher, J.-N. Schmidt, M. Eisenmann, T. Langen, T. Pfau, and I. Ferrier-Barbut, Phys. Rev. Lett. **121**, 030401 (2018).
[9] H. Kadau, M. Schmitt, M. Wenzel, C. Wink, T. Maier, I. Ferrier-Barbut, and T. Pfau, Nature (London) **530**, 194 (2016).
[10] I. Ferrier-Barbut, H. Kadau, M. Schmitt, M. Wenzel, and T. Pfau, Phys. Rev. Lett. **116**, 215301 (2016).
[11] F. Böttcher, J.-N. Schmidt, J. Hertkorn, K. S. H. Ng, S. D. Graham, M. Guo, T. Langen, and T. Pfau, Rep. Prog. Phys. **84**, 012403 (2021).
[12] L. Tanzi, E. Lucioni, F. Famà, J. Catani, A. Fioretti, C. Gabbanini, R. N. Bisset, L. Santos, and G. Modugno, Phys. Rev. Lett. **122**, 130405 (2019).
[13] F. Böttcher, J.-N. Schmidt, M. Wenzel, J. Hertkorn, M. Guo, T. Langen, and T. Pfau, Phys. Rev. X **9**, 011051 (2019).
[14] L. Chomaz, D. Petter, P. Ilzhöfer, G. Natale, A. Trautmann, C. Politi, G. Durastante, R. M. W. van Bijnen, A. Patscheider, M. Sohmen, M. J. Mark, and F. Ferlaino, Phys. Rev. X **9**, 021012 (2019).
[15] M. Guo, F. Böttcher, J. Hertkorn, J.-N. Schmidt, M. Wenzel, H. P. Büchler, T. Langen, and T. Pfau, Nature (London) **574**, 386 (2019).
[16] G. Natale, R. M. W. van Bijnen, A. Patscheider, D. Petter, M. J. Mark, L. Chomaz, and F. Ferlaino, Phys. Rev. Lett. **123**, 050402 (2019).
[17] L. Tanzi, S. Roccuzzo, E. Lucioni, F. Famà, A. Fioretti, C. Gabbanini, G. Modugno, A. Recati, and S. Stringari, Nature (London) **574**, 382 (2019).
[18] S. Ronen, D. C. E. Bortolotti, and J. L. Bohn, Phys. Rev. Lett. **98**, 030406 (2007).
[19] R. M. Wilson, S. Ronen, J. L. Bohn, and H. Pu, Phys. Rev. Lett. **100**, 245302 (2008).
[20] R. N. Bisset, D. Baillie, and P. B. Blakie, Phys. Rev. A **88**, 043606 (2013).
[21] J. Hertkorn, F. Böttcher, M. Guo, J.-N. Schmidt, T. Langen, H. P. Büchler, and T. Pfau, Phys. Rev. Lett. **123**, 193002 (2019).
[22] L. Chomaz, R. M. Van Bijnen, D. Petter, G. Faraoni, S. Baier, J. H. Becher, M. J. Mark, F. Wächtler, L. Santos, and F. Ferlaino, Nat. Phys. **14**, 442 (2018).
[23] D. Petter, G. Natale, R. M. W. van Bijnen, A. Patscheider, M. J. Mark, L. Chomaz, and F. Ferlaino, Phys. Rev. Lett. **122**, 183401 (2019).
[24] J. Hertkorn, J.-N. Schmidt, F. Böttcher, M. Guo, M. Schmidt, K. S. H. Ng, S. D. Graham, H. P. Büchler, T. Langen, M. Zwierlein, and T. Pfau, Phys. Rev. X **11**, 011037 (2021).
[25] C.-L. Hung, X. Zhang, L.-C. Ha, S.-K. Tung, N. Gemelke, and C. Chin, New J. Phys. **13**, 075019 (2011).
[26] S. Ronen, D. C. E. Bortolotti, and J. L. Bohn, Phys. Rev. A **74**, 013623 (2006).
[27] See Supplemental Material at http://link.aps.org/supplemental/10.1103/PhysRevLett.126.193002 for further details on the experiment, analysis, and simulation, which includes Refs. [28–43].
[28] K. Baumann, N. Q. Burdick, M. Lu, and B. L. Lev, Phys. Rev. A **89**, 020701(R) (2014).
[29] T. Maier, I. Ferrier-Barbut, H. Kadau, M. Schmitt, M. Wenzel, C. Wink, T. Pfau, K. Jachymski, and P. S. Julienne, Phys. Rev. A **92**, 060702(R) (2015).
[30] T. Maier, H. Kadau, M. Schmitt, M. Wenzel, I. Ferrier-Barbut, T. Pfau, A. Frisch, S. Baier, K. Aikawa, L. Chomaz, M. J. Mark, F. Ferlaino, C. Makrides, E. Tiesinga, A. Petrov, and S. Kotochigova, Phys. Rev. X **5**, 041029 (2015).
[31] A. Frisch, M. Mark, K. Aikawa, F. Ferlaino, J. L. Bohn, C. Makrides, A. Petrov, and S. Kotochigova, Nature (London) **507**, 475 (2014).
[32] E. Lucioni, L. Tanzi, A. Fregosi, J. Catani, S. Gozzini, M. Inguscio, A. Fioretti, C. Gabbanini, and G. Modugno, Phys. Rev. A **97**, 060701(R) (2018).
[33] Y. Tang, A. Sykes, N. Q. Burdick, J. L. Bohn, and B. L. Lev, Phys. Rev. A **92**, 022703 (2015).
[34] Y. Tang, A. G. Sykes, N. Q. Burdick, J. M. DiSciacca, D. S. Petrov, and B. L. Lev, Phys. Rev. Lett. **117**, 155301 (2016).
[35] Y. Tang, W. Kao, K.-Y. Li, S. Seo, K. Mallayya, M. Rigol, S. Gopalakrishnan, and B. L. Lev, Phys. Rev. X **8**, 021030 (2018).
[36] T. Lindeberg, Int. J. Comput. Vis. **11**, 283 (1993).
[37] T. Lindeberg, Int. J. Comput. Vis. **30**, 79 (1998).
[38] M. Wenzel, F. Böttcher, T. Langen, I. Ferrier-Barbut, and T. Pfau, Phys. Rev. A **96**, 053630 (2017).
[39] S. M. Roccuzzo and F. Ancilotto, Phys. Rev. A **99**, 041601 (R) (2019).
[40] R. N. Bisset, R. M. Wilson, D. Baillie, and P. B. Blakie, Phys. Rev. A **94**, 033619 (2016).

[41] D. Baillie, R. M. Wilson, and P. B. Blakie, Phys. Rev. Lett. **119**, 255302 (2017).
[42] J. von Neumann and E. Wigner, Phys. Z. **30**, 467 (1929).
[43] L. Landau and E. Lifshitz, *Quantum Mechanics: Non-Relativistic Theory* (Elsevier Science, Amsterdam, 1981).
[44] A. Gallemí, S. M. Roccuzzo, S. Stringari, and A. Recati, Phys. Rev. A **102**, 023322 (2020).
[45] A. S. Arkhipov, G. E. Astrakharchik, A. V. Belikov, and Y. E. Lozovik, J. Exp. Theor. Phys. Lett. **82**, 39 (2005).
[46] G. E. Astrakharchik, J. Boronat, I. L. Kurbakov, and Y. E. Lozovik, Phys. Rev. Lett. **98**, 060405 (2007).
[47] P. B. Blakie, D. Baillie, and R. N. Bisset, Phys. Rev. A **86**, 021604(R) (2012).
[48] P. B. Blakie, D. Baillie, and R. N. Bisset, Phys. Rev. A **88**, 013638 (2013).
[49] L. Pitaevskii and S. Stringari, *Bose-Einstein Condensation and Superfluidity*, International Series of Monographs on Physics (Oxford University Press, Oxford, 2016).
[50] The $m = 1$ roton modes weakly lose their degeneracy near the transition due to the slightly asymmetric trap used in the simulations. We show the average of the two energies in Fig. 1 and refer to Ref. [27] for further details.
[51] The near degeneracy of the roton modes on the BEC side translates into a complex situation on the crystal side. We find a number of competing ground states reflecting the different symmetries of the rotons. This precludes a further meaningful BdG analysis for the given parameters.
[52] W. Kohn, Phys. Rev. **123**, 1242 (1961).
[53] R. M. Wilson, S. Ronen, and J. L. Bohn, Phys. Rev. A **79**, 013621 (2009).
[54] O. Dutta and P. Meystre, Phys. Rev. A **75**, 053604 (2007).
[55] R. M. Wilson, S. Ronen, and J. L. Bohn, Phys. Rev. A **80**, 023614 (2009).
[56] H. Y. Lu, H. Lu, J. N. Zhang, R. Z. Qiu, H. Pu, and S. Yi, Phys. Rev. A **82**, 023622 (2010).
[57] A. D. Martin and P. B. Blakie, Phys. Rev. A **86**, 053623 (2012).
[58] D. S. Petrov, Phys. Rev. Lett. **115**, 155302 (2015).
[59] C.-L. Hung, V. Gurarie, and C. Chin, Science **341**, 1213 (2013).
[60] J. Esteve, J.-B. Trebbia, T. Schumm, A. Aspect, C. I. Westbrook, and I. Bouchoule, Phys. Rev. Lett. **96**, 130403 (2006).
[61] A. Imambekov, I. E. Mazets, D. S. Petrov, V. Gritsev, S. Manz, S. Hofferberth, T. Schumm, E. Demler, and J. Schmiedmayer, Phys. Rev. A **80**, 033604 (2009).
[62] J. Armijo, T. Jacqmin, K. V. Kheruntsyan, and I. Bouchoule, Phys. Rev. Lett. **105**, 230402 (2010).
[63] T. Jacqmin, J. Armijo, T. Berrada, K. V. Kheruntsyan, and I. Bouchoule, Phys. Rev. Lett. **106**, 230405 (2011).
[64] M. Schemmer, A. Johnson, and I. Bouchoule, Phys. Rev. A **98**, 043604 (2018).
[65] B. Efron, Ann. Stat. **7**, 1 (1979).
[66] R. Schützhold, M. Uhlmann, Y. Xu, and U. R. Fischer, Int. J. Mod. Phys. B **20**, 3555 (2006).
[67] A. R. P. Lima and A. Pelster, Phys. Rev. A **84**, 041604(R) (2011).
[68] A. R. P. Lima and A. Pelster, Phys. Rev. A **86**, 063609 (2012).